

High power selective laser melting of crack sensitive nickel-base alloy CM247LC, including dimensional analysis and modelling

Marcel Gerstgrasser (✉ gerstgrasser@iwf.mavt.ethz.ch)

ETH Zurich: Eidgenössische Technische Hochschule Zurich

Michael Cloots

Raphael Jakob

Josef Stirnimann

Konrad Wegener

Research Article

Keywords: HP SLM, Laser powder bed fusion (LPBF), Crack healing, Re-melting cracks

Posted Date: November 29th, 2021

DOI: <https://doi.org/10.21203/rs.3.rs-1108701/v1>

License:  This work is licensed under a Creative Commons Attribution 4.0 International License.

[Read Full License](#)

1
2 **High power selective laser melting of crack sensitive nickel-base alloy**
3 **CM247LC, including dimensional analysis and modelling**
4

5 Marcel Gerstgrasser^{1*}, Michael Cloots², Raphael Jakob¹, Josef Stirnimann³, Konrad Wegener^{1,3}
6

7 ¹Institute of Machine Tools and Manufacturing, ETH Zurich, Leonhardstrasse 21, 8092 Zurich, Switzerland

8 <http://www.iwf.mavt.ethz.ch>

9 ²IRPD AG, Lerchenfeldstrasse 3, 9014 St. Gallen, Switzerland

10 ³inspire AG, Technoparkstrasse 1, 8005 Zurich, Switzerland
11

12 *Corresponding author: gerstgrasser@iwf.mavt.ethz.ch (M. Gerstgrasser)
13

14 **Keywords:** HP SLM; Laser powder bed fusion (LPBF); Crack healing; Re-melting cracks;

15 **Abstract.**

16 Compared to reference parameters in the low power and scan velocity range, which lead to
17 dense and crack-free CM247LC LPBF samples due to in-situ crack healing, high power, high
18 scan velocities and increased laser beam diameters are investigated, to decrease the production
19 time further. By keeping the maximum laser intensity from the reference and the laser power to
20 scan velocity ratio constant, the intensity approach provides an initial estimation for the laser
21 spot size regarding the measured Archimedean density and crack density in the high power and
22 high scan velocity range. The investigated cracks are identified as re-melting cracks.
23 Solidification or hot cracks are not observed, since the crack healing effect for those kinds of
24 cracks still occurs. Furthermore, a melt pool depth range is discovered, where not only
25 solidification cracks can be avoided, but also re-melting cracks, which are resulting from higher
26 laser power inputs. This theory can be proven by further laser spot size optimization, where the
27 melt pool depth comes closer to the mentioned range. The Archimedean density and crack
28 density results, in case of the 600 W power parameter with 2400 mm/s scan velocity and a beam
29 diameter of 164 μm , are close to the one obtained from the reference with 200 W, a scan velocity
30 of 800 mm/s and a laser spot of 90 μm . With the intensity approach and laser beam diameter
31 optimization, the production time can be reduced by 300%. Based on dimensional analysis, a
32 model, which combines the samples density with the crack density through the melt pool depth,
33 is presented. Six main and two additional process and laser parameters are taken into relation.
34 The result from the model and the measured values from experiments are in good agreement.
35 Additionally, the influence of the doubled layer thickness and an increased hatch distance by
36 50% with varying scan velocities on the Archimedean density and crack density is analysed.

37

1 **1. Introduction**

2 Selective laser melting (SLM) is a synonym for a layer-wise solidification of a deposited
3 powder layer with a laser source. Since standard SLM-processes have an increased production
4 time, two main strategies are found for increasing the productivity, according to Montero-
5 Sistiaga et al. [1]. In the first case, several “standard” lasers are working in parallel, whereas in
6 the second case high power lasers are used for SLM-processing. The last mentioned approach
7 is called High Power SLM (HP SLM).

8 Most studies about HP SLM are based on steel powders. With a laser power of 380 W
9 compared to 100 W, the laser scan speed can be enhanced by approximately 3.8 times, which
10 increases the build rate about 72% in case of SS316L (1.4404 steel), as reported by Sun et al.
11 [2]. A direct relationship between the laser power input and the build rate is identified. The
12 influence of high laser powers up to 800 W in conjunction with strongly increased beam
13 diameters up to 262 μm , in case of SS316L, is investigated in the research of Metelkova et al.
14 [3]. The combination of laser defocusing and high power inputs increases the productivity up
15 to 840%. In the study of Montero-Sistiaga et al. [1], HP SLM of SS316L with a 1 kW top hat
16 power distribution laser and a beam radius of 700 μm is analysed. Independent of the applied
17 scan strategy, meaning different rotation angle between the layers, cracks occurred parallel to
18 the build direction in all SS316L samples during HP SLM with a top hat. By varying the laser
19 power from 80 to 480 W and the scan velocity from 493 to 2958 mm/s, a minimum energy
20 density of about 9.34 J/mm³ is identified to guarantee relative densities over 99.5% in case of
21 SS316L, as reported by Bang et al. [4]. At a fixed power of 400 W, the microstructural
22 properties, the mechanical properties and the chemical composition changes with varying
23 energy density from 9.58 to 47.95 J/mm³. By upscaling from a laser power between 100 to 300
24 W and spot size of 80 μm , stable single tracks are formed at 900 W and a beam diameter of 240
25 μm in case of a 17-4PH steel powder (AISI 630), as explained in the research of Makoana et
26 al. [5]. The geometrical characteristics of the single tracks are mainly affected by the laser
27 power and scan speed. Furthermore, the layer thickness is identified as an unpredictable
28 parameter, since small changes result in an unstable mode to form single tracks. This will lead
29 to larger fraction of porosity and 3D parts cannot be completed. By analysing the microstructure
30 of HP SLM-processed 24CrNiMoY alloy steel with a laser power of 2 kW and a beam diameter
31 of 4 mm, granular bainite and lath bainite are identified as the mainly contents, according to
32 Zuo et al. [6]. The 24CrNiMoY samples are dominated by high-angle grain boundaries. In case
33 of 300 M steel, a modified AISI 4340, the theoretical build-up rate increases from 3.2 to 28.8
34 mm³/s, by scaling up the laser power from 300 to 1900 W and ensuring high relative density of
35 the SLM-processed samples, as reported by Jing et al. [7]. At higher laser power values of 800
36 to 1900 W, a keyhole mode with “U” shape is observed, compared to semi-elliptical shapes at
37 lower laser power. The melt pool depth increases with increased laser power.

1 However, several defects and problems are investigated with HP SLM in case of steel
2 powders. Based on an instrumented setup with laser power from 150 to 1600 W, a beam
3 diameter of 200 μm (top hat) and scan velocities between 330 to 750 mm/s, several experiments
4 and physical phenomena are analysed in the study of Gunenthiram et al. [8]. Such phenomenon
5 are dynamic instabilities of the melt pool, microparticles and macropatters formation and
6 ejection, and powder denudation effects around the tracks. Vaporization effects, which are
7 located near the laser-melt pool interaction zone, are identified as the main driving force and
8 provoke the destabilization of the global process. In case of process optimization, such
9 destabilizations play an extensive role. Similar investigations are made in the study of Jing and
10 Wang [9] with single tracks, single layers and block samples of HP SLM-processed 300 M steel
11 (modified AISI 4340) with a laser power of 2 kW and a beam diameter of 278 μm . Three main
12 types of defects are identified, including protrusions, depressions and spatter, which exist on
13 the surface of the prior solidified layers during HP SLM-processing. The protrusion and spatters
14 create instabilities for powder spreading during powder depositing. Lack of fusion voids and
15 unfused powders are resulting from depressions, which make the actual thickness greater than
16 the specified one. Spherical spatters with a size of 105 to 425 μm and irregular spatters with a
17 size of 35 to 115 μm seriously contaminate the previously solidified parts, creating spatter-
18 caused pores and impurities.

19 In case of HP SLM of aluminium alloy AlSi10Mg, imperfections can be avoided with
20 high energy per unit. At 900 W, in conjunction with different scan velocities from 1300 to 2100
21 mm/s, density values above 99.5% can be realized, as reported by Buchbinder et al. [10]. The
22 build rate of approximately 5 mm^3/s can be increase to 21 mm^3/s for HP SLM of AlSi10Mg.
23 The laser beam intensity profile has been identified as one important process parameter for HP
24 SLM of AlSi10Mg, as investigated in the research of Wischeropp et al. [11]. The process
25 window, which produces high densities above 99.5%, is larger for the Donut beam profile than
26 that for the Gaussian beam profile. Different defocus distances from -7 mm to 4 mm at 285 W
27 and varying laser powers from 240 W to 285 W at a constant defocus distance of -3 mm are
28 investigated by Rashid et al. [12], in case of SLM-processing of AlSi12. A focus distance of -
29 3 mm and a laser power of 285 W are identified as an optimum for the measured density values.

30 Two different beam diameter, 50 μm and 200 μm , and a laser power of 400 W were
31 used to fabricate SLM-processed Ti-6Al-4V parts with a layer thickness of 200 μm , as reported
32 in the study of Shi et al. [13]. With an increased beam diameter of 200 μm , density values of
33 99.95% can be reached. 16 different combinations of defocused experimental process
34 parameters for Ti-6Al-4V with a power range from 100 W to 370 W, a velocity range from 200
35 mm/s to 2000 mm/s and beam diameters from 100 μm to 260 μm , were investigated by
36 Soylemez [14]. To prevent voids in SLM single beads, a critical melt pool depth to width ratio
37 of 0.85 was found. In the study of Mathe et al. [15], cylindrical specimen for tensile testing

1 were manufactured with a 5 kW laser power, a layer thickness of 50 μm , a preheating
2 temperature of 200 $^{\circ}\text{C}$ and varying energy input from 51 J/mm^3 to 79 J/mm^3 . With those process
3 parameters, densities above 99% were realized. The lowest porosity was measured with the
4 highest analysed energy input of 79 J/mm^3 .

5 A few studies are found in case of HP SLM with nickel-base alloys. Montero-Sistiaga
6 et al. [16] have analysed the influence of a high power laser with a maximum output of 1 kW
7 and a large beam diameter of 700 μm with a top-hat power distribution on Hastelloy X. The
8 observed cracks are significantly longer and have an average crack length of around 150 μm ,
9 compared to lower laser power with a spot size of 70 μm (Gaussian power distribution) and an
10 average crack length of 36 μm . Based on HP SLM-processed Inconel 718 samples with
11 prismatic dimensions, the fully dense forming process window becomes narrower as the laser
12 power increases from 500 W to 2000 W, according to Yang et al. [17]. The build rate increases
13 from 6 mm^3/s to 14.3 mm^3/s , which is 2.38 times faster. The influence of three different types
14 of beams, 200 W Gaussian beam, 2 kW Gaussian beam and 6 kW square-shaped flat-top beam,
15 on the microstructure and texture are investigated in the research of Wang and Shi [18]. In case
16 of the ultra-high power (UHP) SLM with the 6 kW laser beam, the grain size increases 150%
17 and the grains are elongated to millimetre-scale along the build direction, compared to the 200
18 W Gaussian beam. Interestingly, the weakest texture is observed with the 2 kW Gaussian beam.
19 Based on single tracks with to different laser beam configurations, including a beam diameter
20 of 80 μm with varying laser power from 200 W to 800 W and a beam diameter of 500 μm with
21 1000 W, optimal process parameters are identified to manufacture SLM-processed cubic
22 Inconel 625 samples, as explained in the research of Sow et al. [19]. In case of process stability,
23 spatter reduction and part density, the use of the larger beam provides significant improvements
24 due vaporization reduction. The build rate could only be improved moderately (up to 8 mm^3/s).

25 In addition, several problems are investigated in case of HP SLM of nickel-base alloy
26 Inconel 718 with laser powers from 350 W to 1550 W, as explained in detail in the study of Yin
27 et al. [20]. With an increase in laser energy input, the fluctuation of the melt pool is more
28 intensive. A droplet column, which is an advanced form of droplet spatters, occurs more likely
29 with high laser power. Furthermore, large spatter tend to be generated also with a high-power
30 laser. The melt pool instability, the collision of spatters and the powder agglomeration are the
31 dominant mechanisms for large spatters.

32 In the current study, HP SLM of nickel-base alloy CM247LC is investigated. The major
33 difficulty during SLM-processing of precipitation-hardened nickel-base alloys, especially
34 CM247LC, is their high susceptibility to hot cracking, as reported by Carter et al. [21]. Based
35 on reference parameters with 200 W, which results in dense and crack free CM247LC samples,
36 high power and high scan velocity parameters are re-scaled and optimized to decrease

1 production time further with similar results regarding Archimedean density and crack density,
 2 as obtained from the reference samples. The reference process and laser parameters for dense
 3 and crack-free CM247LC are described in detail in the research of [22] and summarized in the
 4 study of [23]. To increase the productivity further, all samples are manufactured with a bi-
 5 directional scan strategy. Furthermore, a relation between the relative density and crack density
 6 over the melt pool depth is found, based on Buckingham's Π -theorem for dimensional analysis
 7 and modelling. Additionally, the influence of double the layer thickness on the Archimedean
 8 density and crack density is analysed, based on the mentioned re-scale approach. To further
 9 increase the productivity, an increased hatch distance of 50% is investigated, in conjunction
 10 with the doubled layer thickness.

11

12 2. Experimental and modelling approach

13 2.1. Selective laser melting setup

14 A powder batch from LPW Technology Ltd with a d_{50} of 40 μm is used in conjunction
 15 with a modularly constructed and vacuum suitable SLM laboratory machine, which includes a
 16 continuous wave fiber laser type IPG YLR-1000-WC with a wavelength of 1070 nm. The
 17 chemical compositions of the CM247LC powder are presented in Table 1. The laser source and
 18 the scanning head are water cooled and the coolant is kept constant at a temperature of 22.5 °C.
 19 N_2 is used as shielding gas with an average O_2 content of 0.6% during SLM-processing of
 20 CM247LC. Further information about the SLM laboratory machine can be found in the research
 21 of Wirth et al. [24] and Gutknecht et al. [25].

22 **Table 1**

23 Chemical composition of SLM-processed CM247LC powder (wt. %)

C	Cr	Co	W	Mo	Ta	Al	Ti	Hf	B	Zr	Ni
0.06	8.4	9.4	9.6	0.5	3.3	5.6	0.8	1.4	0.01	0.009	Bal

24 2.2. Sample analysis

25 The relative Archimedean density and crack density of the XY plane of the cubic samples
 26 with the dimensions of 10 x 10 x 10 mm^3 are equally measured as in the study of Gerstgrasser
 27 et al. [22]. For each high power parameter with the corresponding scan velocity, three cubic
 28 samples are manufactured. Additionally, fifty melt pool cross-sections of the last layer in the
 29 build up plane (XZ plane) are quantified and analysed for each high power parameter, including
 30 the reference at 200 W with a bi-directional scan strategy. All images are taken with a Keyence
 31 VHX-5000 and quantified with ImageJ.

1

2 2.3. Process parameters and intensity Approach

3 Based on dense and crack-free reference samples in conjunction with the corresponding
 4 process parameters at 200 W with a beam diameter of 90 μm , as explained in the research of
 5 [22] and summarized in the study of [23], the bi-directional scan strategy is applied, not only
 6 to reduce the process time further, but also for the comparison with the high power parameter
 7 samples, manufactured with 500 and 600 W. By using the same peak intensity and the same
 8 track energy density, as known from the crack-free reference samples, higher laser powers and
 9 scan velocities should be achieved with nearly equal results as under the circumstances of the
 10 reference, by simply changing the laser beam diameter in the build plane. Since crack healing
 11 is dependent on the melt pool geometry, especially in case of the melt pool depth, similar melt
 12 pool dimensions have to be achieved, as obtained from the reference. The intensity distribution
 13 for a Gaussian beam is defined as follows, according to Poprawe et al. [26]:

$$I(r_{dis}, z) \equiv I_0(z) e^{-\frac{2r_{dis}^2}{w(z)^2}} \quad (1)$$

14

15 with the following definition of the peak intensity $I_0(z)$ on the beam axis:

$$I_0(z) = \frac{2P}{\pi \cdot w(z)^2} \quad (2)$$

16 where r_{dis} is the radial distance, according to Koechner [27], and $w(z)$ is the beam radius of the
 17 Gaussian beam at a position z , as explained in detail by Poprawe et al. [26]. The intensity
 18 distribution of a Gaussian beam is illustrated in Fig. 1, where the beam radius encloses an area
 19 of 86% of the total beam power. At the beam waist, where the phase front is planar, the Gaussian
 20 beam contracts to the minimum radius, as reported by Koechner [27]. Hence, the maximum
 21 intensity can be expressed as follows, based on the minimum radius w_0 in the confocal region
 22 of a Gaussian beam, where the hyperbolic beam waist is near $z = 0$:

$$I_{\max} = \frac{2P}{\pi \cdot w_0^2} \quad (3)$$

23 where I_{\max} is defined as the maximum or peak Intensity in the focal plane, i.e. $I_0(z = 0)$.

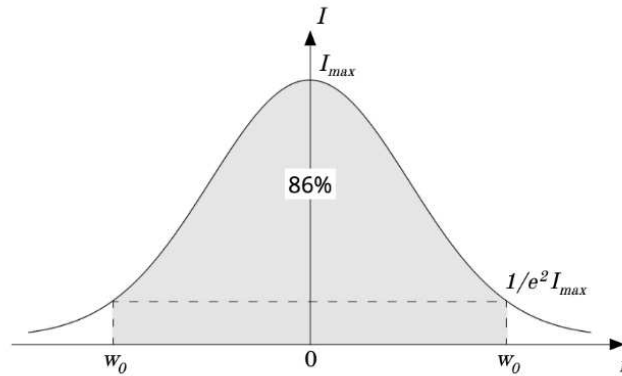


Fig. 1: Gaussian intensity distribution, adapted from Poprawe et al. [26]

In case of the mentioned reference with a laser power of 200 W and a beam diameter of 90 μm ($w_0 = 45 \mu\text{m}$), I_{max} reaches a value of 62.876 kW/mm². To realize crack healing and similar melt pool depths for higher laser power and scan velocity values, the same peak intensity I_{max} is taken as known from the reference samples and the beam diameter is reckon back, as follows:

$$D_p = \sqrt{\frac{8P}{\pi \cdot I_{\text{max}}}} \quad (4)$$

where D_p is the power dependent laser beam diameter in the focus plane, based on the value of laser power P . Based on the track energy density from the reference, which is also kept constant, the corresponding high laser scan velocity is calculated as follows:

$$v_p = \frac{P}{E_t} \quad (5)$$

where v_p is the power dependent laser scan velocity in mm/s, E_t is the track energy density in J/mm and has a value of 0.25 J/mm, as obtained from the reference samples. In case of SLM-processed CM247LC, equation (5) can be written as follows:

$$v_p = P \cdot 4 \frac{\text{mm}}{\text{J}} \quad (6)$$

where the proportionality factor has the unit mm/J.

2.4. Dimensional analysis and modelling

The Rosenthal equation is well-known and a widely used analytical model, not only to describe the weld pool geometry in case of welding, but also the melt pool dimensions in AM, especially for SLM, as reported by Mosallanejad et al. [28]. Originally, the analytical model from Rosenthal [29] was developed to predict the temperature history in fusion welding, as explained by Promopattum et al. [30]. The predicted melt pools are described by a moving heat source, as reported in [28]. The analytical Rosenthal equation can be expressed as follows, according to Tang et al. [31]:

$$T_f = T_0 + \frac{Q}{2\pi k_{th} r_s} \exp\left[-\frac{v_{scan}(\xi_m + r_s)}{2\alpha_d}\right] \quad (7)$$

where the melting point of the alloy is described by T_f , the temperature far from the melt pool is presented by T_0 , the absorbed power is Q , the thermal conductivity of the alloy has the letter k_{th} , the beam speed is defined with v_{scan} and the thermal diffusivity is given by α_d , as reported by Tang et al. [31]. ξ_m represents the laser movement along the x-axis with the moving coordinate of $x - v_{scan} t$ and r_s is the distance from the heat source with $(\xi_m^2 + y^2 + z^2)^{0.5}$, as explained by Promopattum et al. [30]. It has to be mentioned, that the Rosenthal equation does not consider temperature-dependent material properties. Therefore, properties at room temperature are used. A simplified expression of the Rosenthal equation, to estimate the melt pool width for different alloys, which have relatively low thermal diffusivities, such as nickel-base alloy Inconel 718, as reported by Promopattum et al. [30], is deduced by Tang et al. [31]:

$$w \approx \sqrt{\frac{8Q}{e\pi\rho c_p(T_f - T_0)v_{scan}}} \quad (8)$$

where e is the Euler's number, ρ is the density, c_p is the specific heat and Q can be expressed as $\lambda_{ab} P$, according to Promopattum et al. [30]. λ_{ab} is the absorptivity and P is the power. Since semi-circular melt pools are predicted, the estimated melt pool depth is half of the melt pool width, as reported by Promopattum et al. [30]:

$$d \approx \sqrt{\frac{2 \lambda_{ab} P}{e \pi \rho c_p (T_f - T_0) v_{scan}}} \quad (9)$$

1 Equation (9) demonstrates, that the melt pool dimensions are proportional to the square root of
 2 the laser power to scan velocity ratio, as discussed by Mosallanejad et al. [28]. Since the laser
 3 power to scan velocity ratio is kept constant for re-scaling in this research, as mentioned in
 4 section 2.4, the same melt pool depths are proposed, independent of the power or scan speed
 5 values. Furthermore, the intensity or power density, which is a function of the laser beam
 6 diameter and is needed to explain the experimental observations in a proper way, has to be
 7 considered. Additionally, not only a relation between the melt pool depth to density is required,
 8 but also to the crack density.

9 In the recent research of Khan et al. [32], Estrada-Díaz et al. [33] and Estrada-Díaz et
 10 al. [34], the melt pool depth or density for SLM-processed samples are predicted with
 11 dimensional analysis by applying the Buckingham's Π -theorem. The relation between melt
 12 pool depth, density and crack density is still missing. Nevertheless, Buckingham's Π -theorem
 13 provides a possibility to find reasonable relations between the influence parameters of the
 14 process. A physical phenomenon can be described by k number of independent variables, such
 15 as $x_1, x_2, x_3, \dots, x_k$, as explained in detail by Zohuri [35]. The phenomenon can be analytically
 16 expressed as follows:

$$f(x_1, x_2, x_3, \dots, x_k) = 0 \quad (10)$$

17 which is a unit free physical law and represents any mathematical equation in Physics and
 18 Engineering with k dimensional variables of l fundamental units, according to Jazar [36]. Such
 19 fundamental units or dimensions are length [L], time [T], mass [M], etc. In terms of $k-l$
 20 independent dimensionless groups, the phenomenon can be described by Π -terms, as explained
 21 by Zohuri [35]. By using Buckingham's Π notation, the famous Π -theorem, to represent a
 22 dimensionless term, can be expressed as follows, according to Dym [37]:

$$\Pi_1 = \Phi(\Pi_2, \Pi_3, \dots, \Pi_{k-l}) \quad (11)$$

23 or equivalently:

$$\Phi(\Pi_1, \Pi_2, \Pi_3, \dots, \Pi_{k-l}) = 0 \quad (12)$$

24 The Π -terms are formed by the product of the variables $x_1, x_2, x_3, \dots, x_l$ raised to the unknown
 25 integer exponents a for each Π -term (excluding the $k-l$ variables), according to Zohuri [35]:

$$\begin{aligned}
\Pi_1 &= x_1^{a_{1,1}} x_2^{a_{1,2}} \dots x_l^{a_{1,n}} x_{l+1} \\
\Pi_2 &= x_1^{a_{2,1}} x_2^{a_{2,2}} \dots x_l^{a_{2,n}} x_{l+2} \\
&\dots \\
\Pi_{k-l} &= x_1^{a_{(k-l),1}} x_2^{a_{(k-l),2}} \dots x_l^{a_{(k-l),n}} x_k
\end{aligned} \tag{13}$$

1 The integer exponents $a_{i,n}$ are different for each Π -term. Since the Π -terms are
2 dimensionless, the exponent of all the fundamental dimensions have to be zero. This leads to a
3 linear equation system with l number of equations, as reported by Zohuri [35]. Meaningful
4 information and detailed examples about the Buckingham's Π -theorem can be found in the
5 definitive books of Dym [37] and Zohuri [35].

7 2.5. Increased layer thickness and hatch distance

8 In case of doubling the layer thickness and increased hatch distance of 50%, only one
9 cubic sample for each parameter is produced, to reduce effort and to test the intensity approach
10 with reasonable outlay also for the last two mentioned process parameters with decreasing scan
11 velocity. The Archimedean density and crack density are equally measured as explained in
12 section 2.2.

14 3. Results and discussion

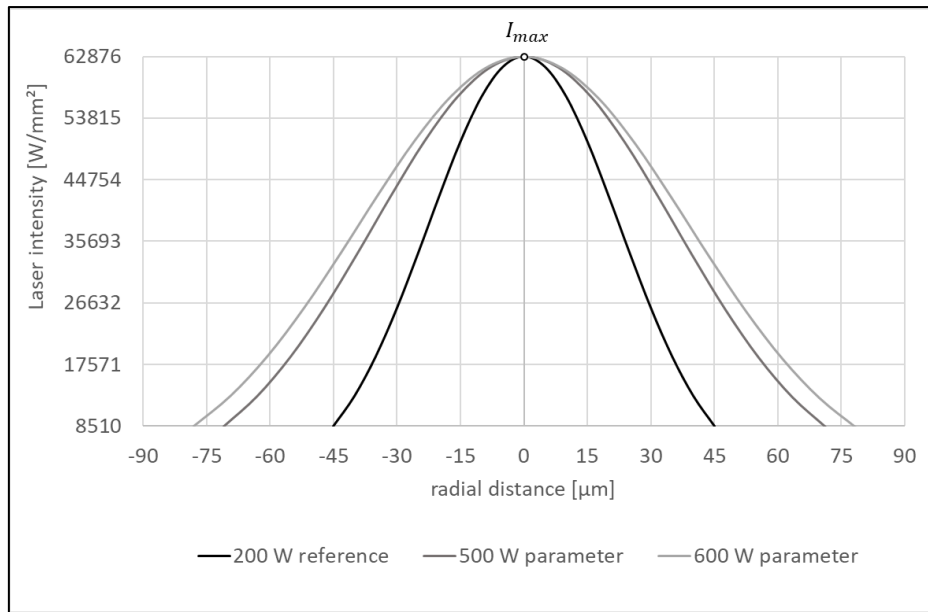
15 3.1. Re-scaled high power and scan velocity parameters

16 Based on equation (4) and (6), the laser beam diameter and scan velocity can be directly
17 obtained from the selected higher power values. In this study, the power values of 500 W and
18 600 W, which are 2.5 and 3 times higher compared to the reference, are investigated with the
19 intensity approach. The re-scaled parameters are summarized in Table 2. Since the track energy
20 E_l is kept constant, also the scan velocity increases 2.5 and 3 times, in case of 500 and 600 W,
21 respectively.

22 Table 2: re-scaled parameters for 500 W and 600 W

Laser power	500 W	600 W
Beam diameter	142 μm	156 μm
scan velocity	2000 mm/s	2400 mm/s

1 The Gaussian intensity distributions of the 200 W reference, the 500 W and 600 W parameter
 2 with the maximum or peak intensity I_{max} of 62876 W/mm² are presented in Fig. 2, based on
 3 equation (1). The corresponding beam radius can be taken from the abscissa, where the intensity
 4 value drops to $1/e^2$ of I_{max} , which has a value of approximately 8510 W/mm².



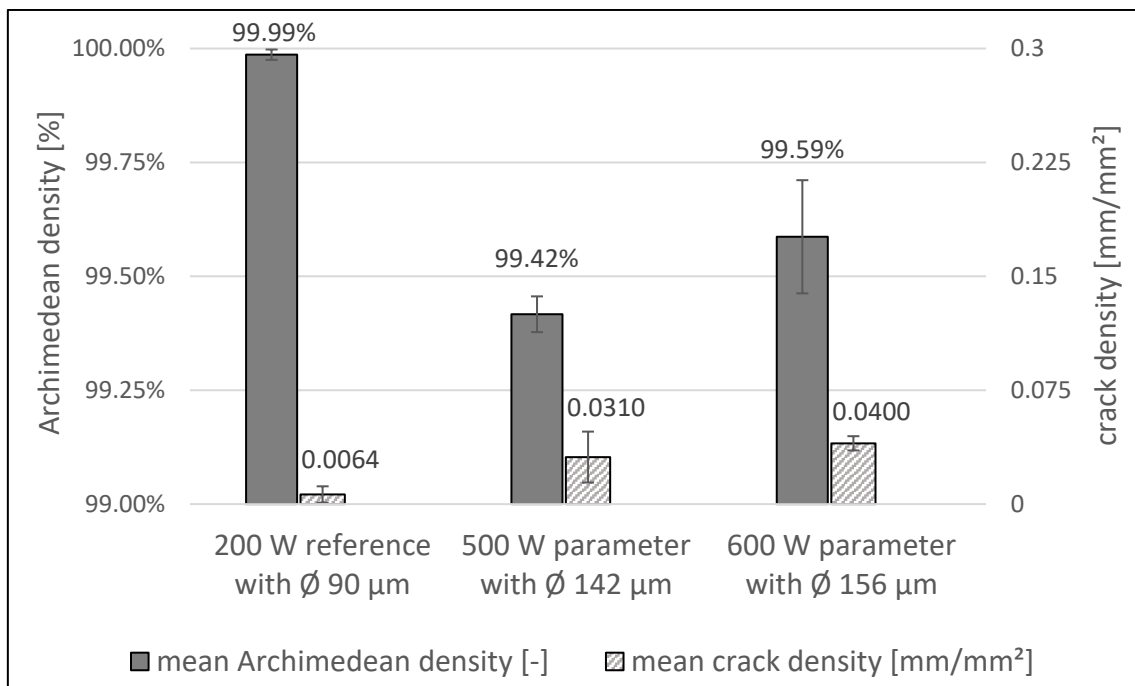
5

6 Fig. 2: Gaussian intensity distributions with peak intensity of the reference parameter and the two higher
 7 power parameters, based on the intensity approach

8 It has to be mentioned that the energy density defined by Mahamood et al. [38] with the unit
 9 J/mm², where the laser power is divided by both the scan velocity and the beam diameter, is not
 10 constant. The quantified results of the obtained Archimedean density as well as the crack
 11 density from the 200 W reference with a beam diameter of 90 µm, the 500 W parameter with a
 12 beam diameter of 142 µm and the 600 W parameter with a beam diameter of 156 µm are shown
 13 in Fig. 3 with the corresponding column chart. Three cubic samples were manufactured and
 14 measured for each mentioned parameter. The obtained standard deviations represent the
 15 corresponding error bars. In case of the bi-directional reference with 200 W, similar
 16 Archimedean density and crack density values are obtained as with the uni-directional
 17 reference, which lead to dense and crack-free samples, as explained in section 2.3. In Fig. 4 a)
 18 half of the analysed XY plane of a sample, manufactured with the 200 W, a scan velocity of
 19 800 mm/s (bi-directional scan strategy) and beam diameter of 90 µm, is shown. Cracks are not
 20 observed and only a few mini-pores are visible, compared to the XY plane, manufacture with
 21 the same power and scan velocity (uni-directional strategy) and a beam diameter of 116 µm, as
 22 explained in detail by Gerstgrasser et al. [22]. Considering not only the average Archimedean
 23 density in Fig. 3, but also the corresponding error bars, the 600 W parameter with Ø 156 µm

1 performs better in comparison to the 500 W parameter with \varnothing 142 μm . Since the crack density
 2 error bars of the 500 W parameter are more extensive than the ones from the 600 W parameter,
 3 results of the measured crack density are similar.

4



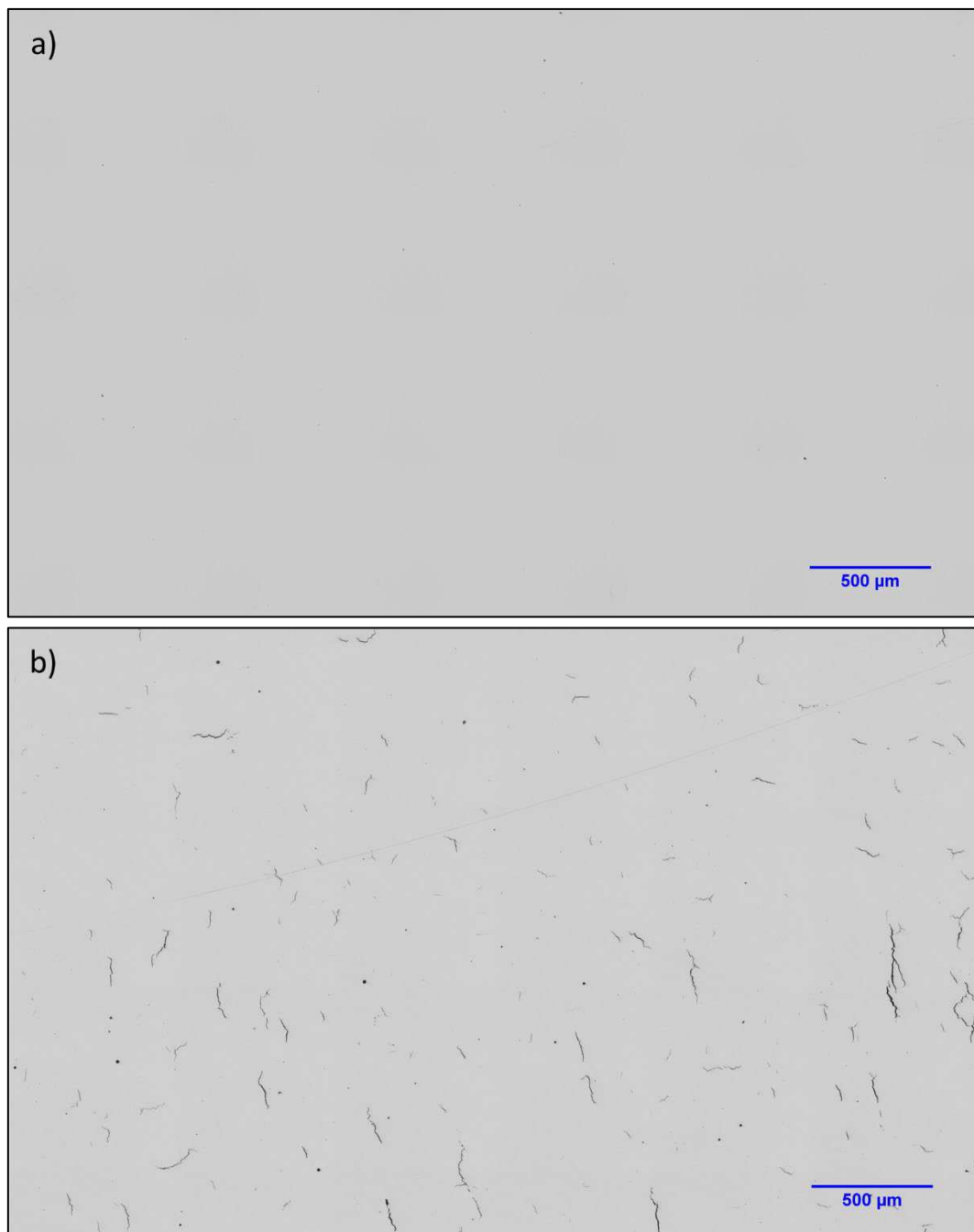
5

6

7

Fig. 3: Results from the defect analysis of the 200 W, 500 W and 600 W parameter with the corresponding beam diameter

8



2

3 Fig. 4: half of the analysed XY plane: a) image, based on the 200 W parameter with a scan velocity of 800 mm/s
4 and a beam diameter of 90 μm. No cracks are observed and a high density can be identified.

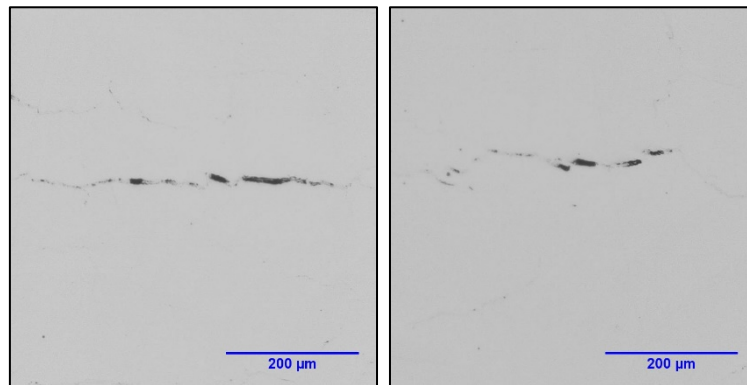
5 b) image with hot cracks, based on 200 W, scan velocity of 800 mm/s and a
6 beam diameter of 116 μm, as analysed and explained by Gerstgrasser et al. [22]

7

8

1 Further investigations reveal that the cracks in the SLM-processed CM247LC samples,
2 manufactured with the 500 W and 600 W parameter, can be identified and classified as re-
3 melting cracks due to their specific morphology, similar as investigated in the research of
4 Gerstgrasser et al. [23]. The re-melting cracks from the examined XY plane are shown in Fig.
5 5, in case of the 500 W and 600 W parameter, respectively.

6



7

8 Fig. 5: re-melting cracks with their typical morphology: obtained from the XY plane from the 500 W parameter
9 with \varnothing 142 μm (left image) and from the 600 W parameter with \varnothing 156 μm (right image)

10

11 Considering not only the higher average Archimedean density of the 600 W parameter in
12 comparison to the 500 W parameter, but also the fact that the production time is decreased by
13 300%, compared to the reference, the 600 W parameter is favoured and further investigated.
14 The qualitative difference of the melt pool geometry for the 200 W reference and 600 W
15 parameter, which are obtained from digital microscopy, are illustrated in Fig. 6 for the last
16 manufactured layer. The melt pool of the 600 W parameter with a beam diameter of 156 μm
17 are deeper than the ones from the 200 W reference, which explain the occurrence of the re-
18 melting cracks. Interestingly, the melt pools, which are manufactured with the 600 W
19 parameter, have a more wavelike surface structure.

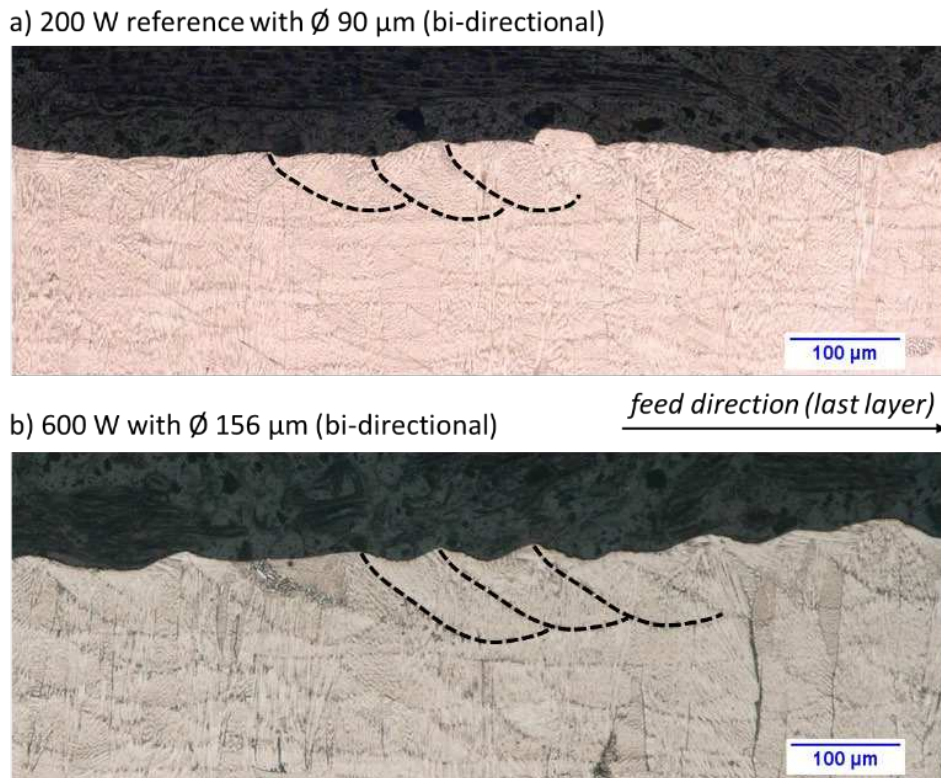
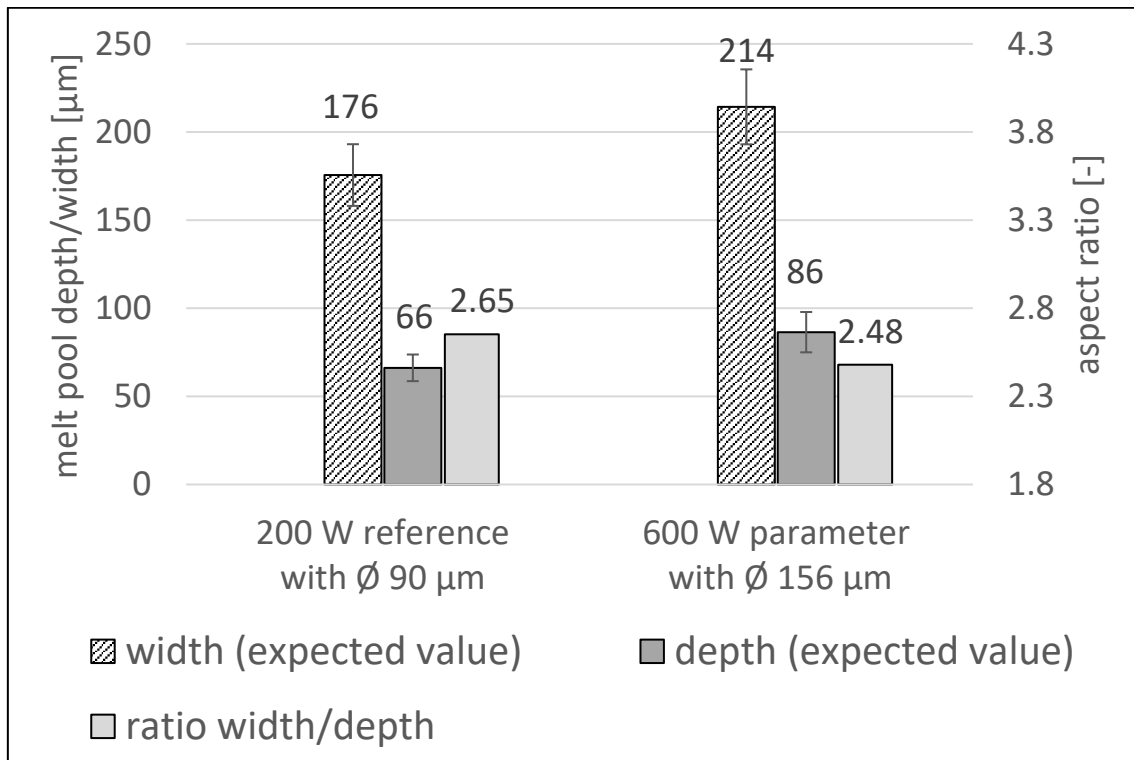


Fig. 6: melt pool geometry from a) the 200 W reference with a beam diameter of 90 μm and
b) the 600 W parameter with a beam diameter of 156 μm

2
3
4
5 Based on fifty measured melt pools for each parameter, the quantified melt pool width
6 (expected values), depth (expected values) and width to depth ratio of the 200 W reference and
7 the 600 W parameter are shown in Fig. 7. The corresponding standard deviations are presented
8 as error bars in the column chart. It seems that the melt pool depth of 66 μm represents a lower
9 crack healing boundary in case for the 200 W reference with a beam diameter of 90 μm and a
10 bi-directional scan strategy. By comparing a depth of 66 μm with the 81 μm from the 200 W
11 reference with a beam diameter of 90 μm and a uni-directional scan strategy, also called hot
12 calibration, where crack healing was realized, and a depth of 59 μm from the 200 W parameter
13 with a beam diameter of 116 μm (cold calibration), where hot cracks occurred, as reported by
14 Gerstgrasser et al. [22], a relative crack healing range for the melt pool depth can be determined.
15 It has to be mentioned that a melt pool depth of 66 μm is rather conservative. The expected
16 value of the melt pool should be in the range from 66 to 81 μm . A few micrometres below a
17 melt pool depth of 66 μm , solidification cracks are occurring, whereas an increased melt pool
18 depth above 81 μm leads to re-melting cracks, due to the deep melt effect in the layers below.
19 Since the melt pool depth from the 600 W parameter with a beam diameter of 156 μm and a
20 scan velocity of 2400 mm/s has a value of 86 (expected value), the beam diameter or the scan

1 velocity has to be increased further, to reach the mentioned crack-free melt pool depth range.
 2 In this study, the increased beam diameter is further investigated.

3



4

5 Fig. 7: quantified melt pool dimensions of the 200 W reference and 600 W parameter,
 6 based on fifty melt pool cross-sections

7

8 3.2. Laser spot size optimization

9 To proof the theory with the widened beam diameter and the required melt pool depth in case
 10 of the 600 W parameter, also two smaller spot diameters, compared to the 156 μm beam size,
 11 are investigated. The analysed beam diameters are 132 μm, 148 μm and 164 μm. The quantified
 12 melt pool geometries for each beam diameter with 600 W and a scan speed of 2400 mm/s are
 13 presented in Fig. 8. The corresponding error bar presents the standard deviation of the fifty
 14 measured melt pools. With an increased laser beam diameter, the melt pool depths are coming
 15 closer to the above-mentioned crack free range, between solidification and re-melting cracks.
 16 The width of the melt pools hardly changes with increasing beam diameter.

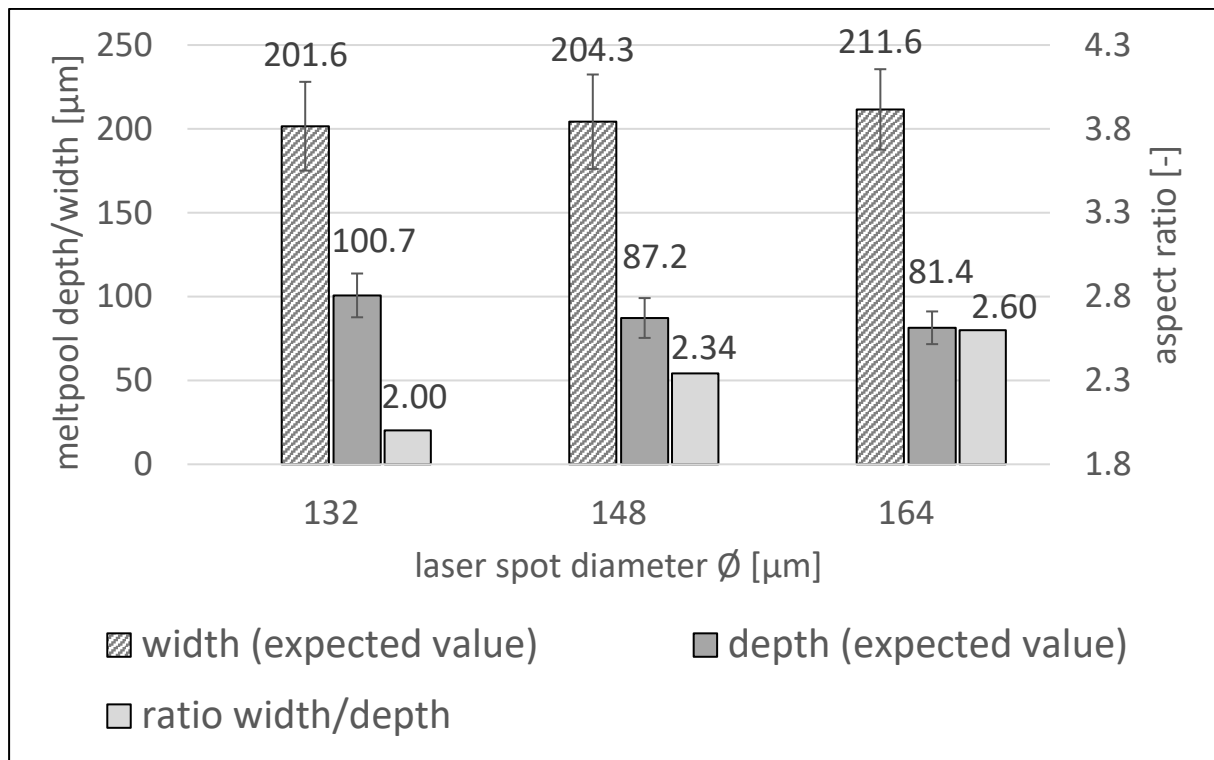


Fig. 8: melt pool geometry analysis of the 600 W parameter with a scan speed of 2400 mm/s and increased laser beam diameter

1
2
3
4
5
6
7
8
9
10
11
12
13
14
15
16
17

The quantified values of the average Archimedean and crack density from the different laser spot diameters, 132, 148 and 164 μm , are shown in Fig. 9. Remarkably, the Archimedean density increases with increased laser spot diameter, whereas the crack density decreases. In case of 600 W, a scan velocity of 2400 mm/s and a beam diameter of 164 μm , the Archimedean and crack density results are coming closer to the values obtained with the 200 W reference, a scan speed of 800 and a beam diameter of 90 μm . The samples manufactured with 600 W, 2400 mm/s and spot size of 164 μm have only a few, small observed re-melting cracks, as presented in Fig. 10 a), based on the sample with the highest measured crack density value in case of the 164 μm laser beam diameter. In case of a 132 μm beam diameter instead of 164 μm , the amount of cracks are drastically higher, as shown in Fig. 10 b) qualitatively. To consider not only the worst-case with a laser power of 600 W, scan speed of 2400 mm/s and a spot size of 164 μm , half of the analysed XY plane from the sample with the smallest measured crack density is presented in Fig. 11 for comparison.

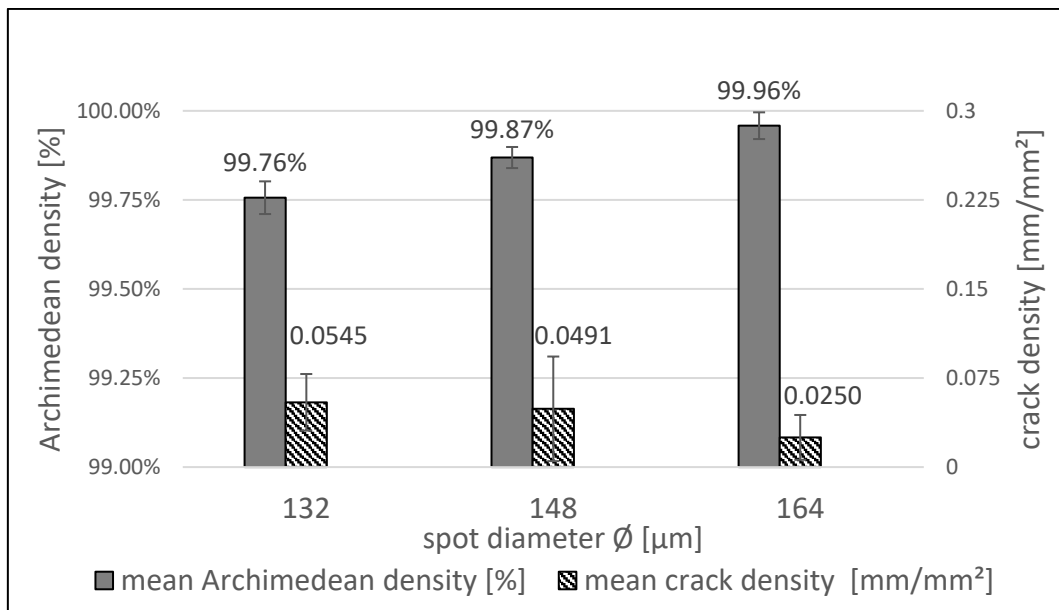
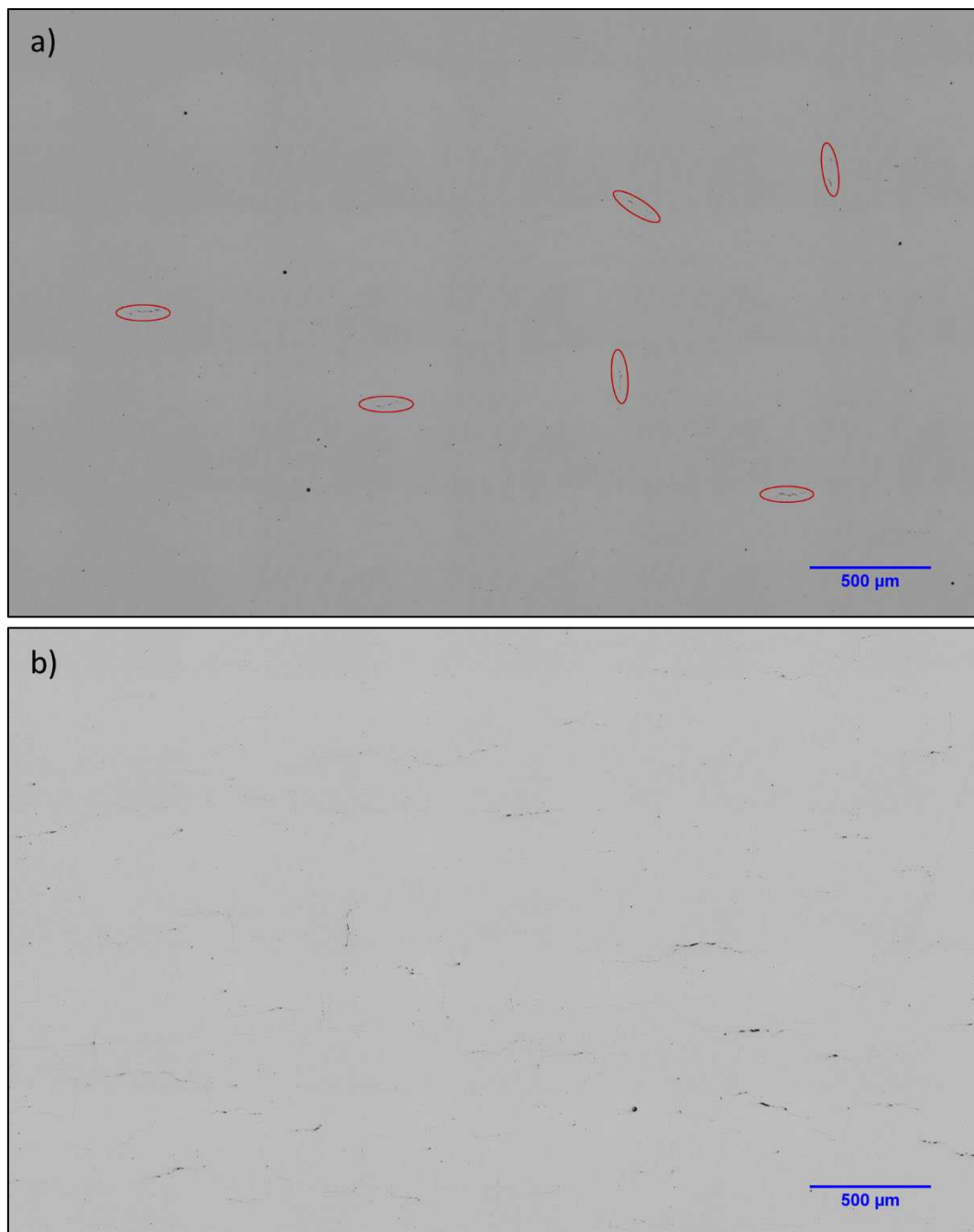


Fig. 9: Results from the defect analysis of the 600 W parameter with a scan velocity of 2400 mm/s and varying laser spot diameters

1
2
3
4



3 Fig. 10: half of the analysed XY plane: a) a few small re-melting cracks in the worst sample with the highest
4 crack density, in case of 600 W, 2400 mm/s and a beam diameter of 164 µm.
5 b) numerous re-melting cracks, in case of a beam diameter of 132 µm



Fig. 11: half of one of the analysed XY plane with the smallest measured crack density, in case of 600 W, 2400 mm/s and a beam diameter of 164 μm

3.3. Crack density model

To explain the experimental observations in section 3.2 with different beam diameters, in case of 600 W and a scan speed of 2400 mm/s, the intensity I , the scan speed v_{scan} and the hatch distance h are defined as fundamental variables. The intensity I is not only a function of the laser power, but also a function of the laser beam diameter and quality. The Buckingham's Π -theorem is applied for two dependent systems, to reduce the complexity and to create reasonable relations with the three remaining variables – sample density ρ_s , melt pool depth d and crack density ρ_{crack} - including the measured results from the experiments in section 3.2. The density ρ_s will be coupled with the crack density ρ_{crack} over the melt pool depth d , which is a key factor for both parameters. The remaining variables are permuted for each of the two systems (1. System: density – melt pool depth; 2. System: melt pool depth – crack density). The parameters, their units and dimensions are summarized in Table 3.

1 Table 3: parameters, their units and fundamental dimensions used for both systems

parameter	unit	dimensions
Intensity I	$\text{W}/\text{mm}^2 = \text{kg}/\text{s}^3$	$M \cdot T^{-3}$
Scan velocity v_{scan}	mm/s	$L \cdot T^{-1}$
Hatch distance h	mm	L
Melt pool depth d	mm	L
Sample density ρ_s	kg/mm^3	$M \cdot L^{-3}$
Crack density ρ_{crack}	$\text{mm}/\text{mm}^2 = 1/\text{mm}$	L^{-1}

2

3 In case of the first system, the fundamental variables are I , v_{scan} and h , which are
 4 permuted with the melt pool depth d and the sample density ρ_s . In this system, the number of
 5 dimensions l has a value of 3 and the amount of variables k is equal to 5, which leads to $k - l = 2$
 6 , meaning two dimensionless Π -terms:

$$\Pi_1 = I^{a_{1.1}} \cdot v_{scan}^{a_{1.2}} \cdot h^{a_{1.3}} \cdot d \quad (14)$$

$$\Pi_2 = I^{a_{2.1}} \cdot v_{scan}^{a_{2.2}} \cdot h^{a_{2.3}} \cdot \rho_s$$

7 Considering the fundamental dimensions for each parameter, the Π -terms can be expressed as:

$$\Pi_1 = \left(\frac{M}{T^3}\right)^{a_{1.1}} \cdot \left(\frac{L}{T}\right)^{a_{1.2}} \cdot L^{a_{1.3}} \cdot L = 1 \quad (15)$$

$$\Pi_2 = \left(\frac{M}{T^3}\right)^{a_{2.1}} \cdot \left(\frac{L}{T}\right)^{a_{2.2}} \cdot L^{a_{2.3}} \cdot \left(\frac{M}{L^3}\right) = 1$$

8 Solving the linear equation system, mentioned in equation (15), for the exponents, the following
 9 two dimensionless Π -terms are identified:

$$\Pi_1 = \frac{d}{h} \quad (16)$$

$$\Pi_2 = \rho_s \frac{v_{scan}^3}{I}$$

1 Using the same procedure for the remaining variables crack density ρ_{crack} and melt pool depth
 2 d in case of the second system, the following two dimensionless Π -terms are determined and
 3 asterisked, to mark the second system:

$$\Pi_1^* = \frac{1}{h \cdot \rho_{crack}} \quad (17)$$

$$\Pi_2^* = \frac{d}{h}$$

4 As mentioned in equation (11), a relation between the two Π -terms for each system has to be
 5 found. Therefore, the process and laser parameter in conjunction with the experimentally
 6 measured Archimedean density, melt pool depth and crack density are used from section 3.2,
 7 to find the corresponding function between each of the Π -terms with curve fitting. Further
 8 information about the least square fit approach for curve fitting can be found in the research of
 9 Gerstgrasser et al. [39]. In case of the first system, a linear relation between the dimensionless
 10 Π_1 and Π_2 -term is observed, as presented in Fig. 12. The associated linear relation of the Π -
 11 terms for the first system can be expressed mathematically as follows:

$$\Pi_1 = C_{1,1} \cdot \Pi_2 + C_{1,2} \quad (18)$$

12 where $C_{1,1}$ and $C_{1,2}$ are the coefficients with a value of -0.16 and 1.7, respectively. The
 13 corresponding residual sum of squares (RSS) or sum of squared estimate of errors (SSE) value
 14 amounts to 0.0020.

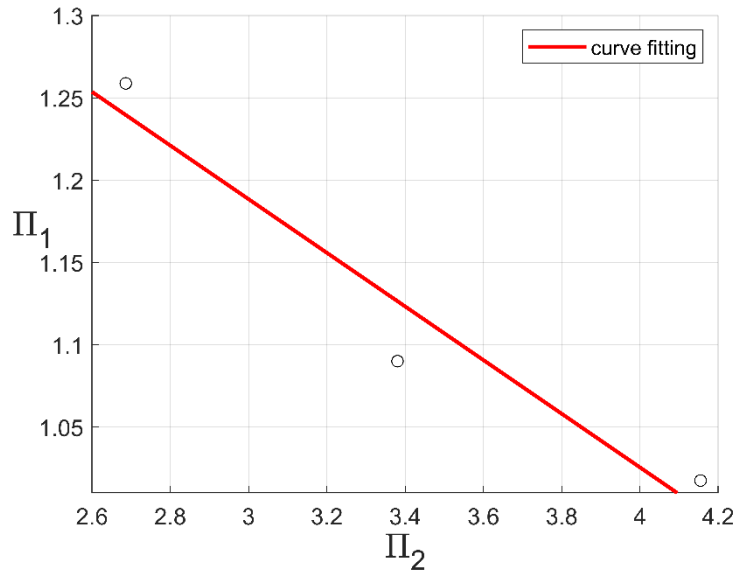


Fig. 12: linear relation between the two dimensionless terms, in case of the first system, based on the experiments from section 3.2

2
3
4

5 By substituting the corresponding variables, including the determined coefficients, and solving
6 for the melt pool depth d , the following equation can be obtained:

$$d = -0.16 \cdot \rho_s \frac{v_{scan}^3}{I} h + 1.7 \cdot h \quad (19)$$

7 Since the Archimedean density is usually the first measured parameter and can be classified as
8 a non-destructive material test, the sample density is defined as an input-parameter, to calculate
9 the melt pool depth. Furthermore, the crack density strongly depends on the melt pool depth, as
10 mentioned in section 3.1.

11 In case of the second system, a power function can be observed between the two
12 dimensionless Π_1^* and Π_2^* -term, as shown in Fig. 13 and expressed as follows:

$$\Pi_1^* = C_{2.1} \cdot (\Pi_2^*)^{C_{2.2}} + C_{2.3} \quad (20)$$

13 where the coefficients $C_{2.1}$, $C_{2.2}$ and $C_{2.3}$ are set to 490, -34 and 229, respectively.

14 Those coefficients lead to a RSS-value of 5.9810×10^{-21} .

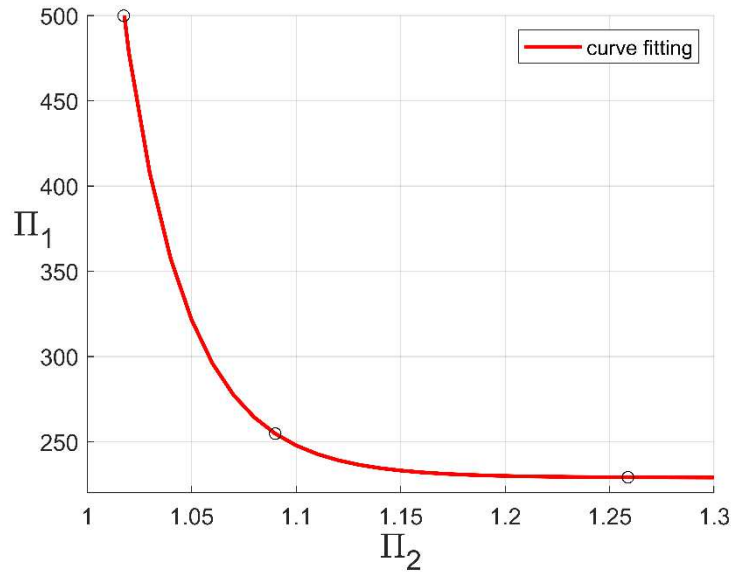


Fig. 13: linear relation between the two dimensionless terms, in case of the second system, based on the experiments from section 3.2

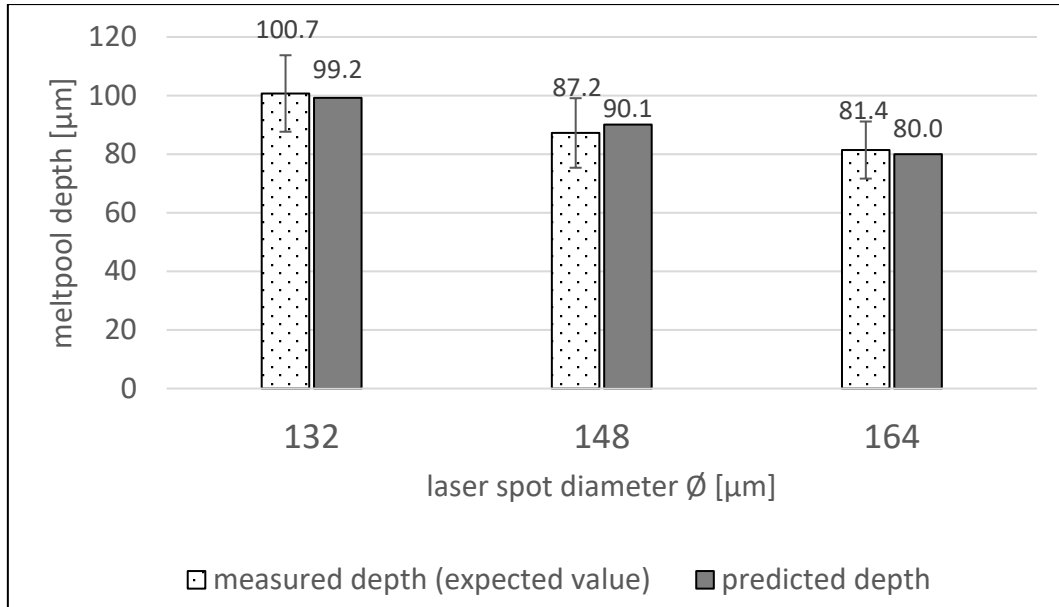
By substituting the corresponding variables, including the three identified coefficients, and solving for the crack density ρ_{crack} , the following equation is determined:

$$\rho_{crack} = \frac{1}{h \cdot \left(490 \cdot \left(\frac{d}{h} \right)^{-34} + 229 \right)} \quad (21)$$

where the relation between the crack density ρ_{crack} and the melt pool depth d is described with equation (21).

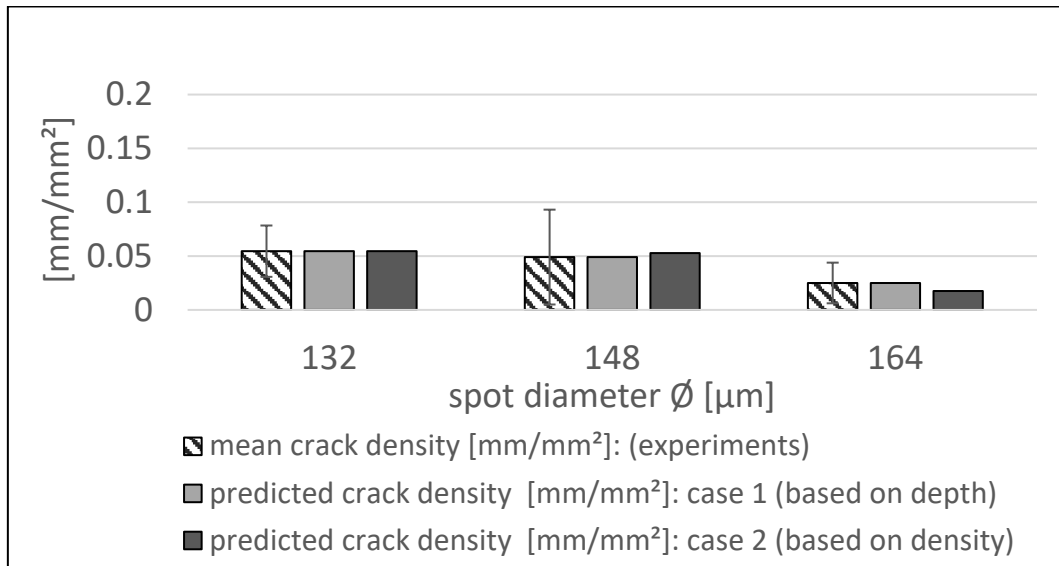
Fifty measured melt pool depths from the experiments are compared to the predicted ones, based on equation (19). As shown in Fig. 14, the results from the experiments and from the model are in good agreement. Regarding the crack density ρ_{crack} , two cases have to be considered. In the first case, the measured melt pool depths from the experiments are taken in conjunction with the process and laser parameters to calculate the crack density ρ_{crack} , based on equation (21). In the second case, the crack density ρ_{crack} is predicted by using the samples density ρ_s with the process and laser parameters. Therefore, both equations, (19) and (21), are connected. Furthermore, the predicted crack densities are compared to the experimentally obtained crack density values. In the first case, the measured crack density values are nearly

1 equal to the predicted crack densities, as shown in Fig. 15. In the second case, which reduces
 2 the amount of work drastically regarding sample preparation and analysis, the predicted crack
 3 densities and the measured ones are also in good agreement.



4
5
6
7

Fig. 14: comparison between measured and predicted melt pool depths, based on the experiments from section 3.2



8
9
10

Fig. 15: comparison between measured and predicted crack density, based on the experiments from section 3.2

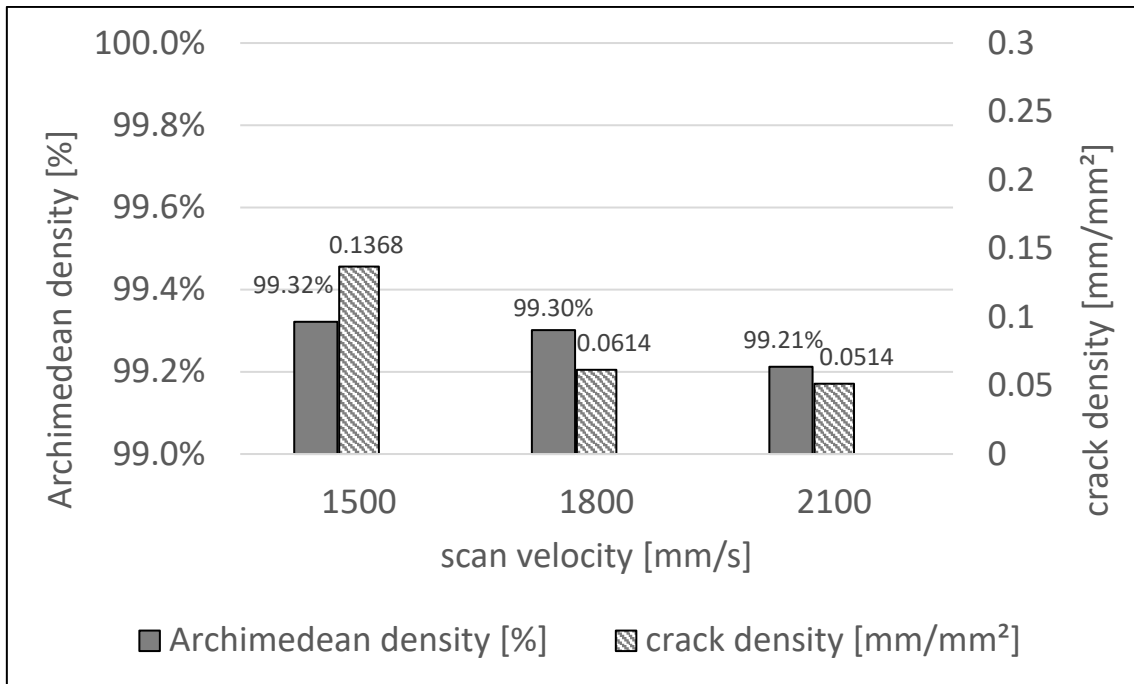
1 Compared to the classic phenomenological modelling with linear regression in case of two
2 parameters, the Buckingham's Π -theorem provides a good alternative to set several process,
3 laser, material and geometrical parameters in relation. In this study, six main and two additional
4 parameters, including the laser power and beam diameter, which are part of the intensity, are
5 taken into relation. Furthermore, Buckingham's Π -theorem is an user-friendly approach to
6 create reasonable models, based on important influence parameters from the process. The low
7 expenditure of time for finding a solution is an additional advantage of this approach. This
8 shows the high potential of dimensional analysis and modelling with the Buckingham's Π -
9 theorem in case of HP SLM regarding sample density and crack density.

10

11

12 **3.4. Influence of increased layer thickness and hatch distance**

13 Using the intensity approach, as explained and discussed in section 2.3 and 3.1, for
14 further investigations regarding increased layer thickness with gradually decreased scan
15 velocity values, interesting results can be obtained in case of Archimedean density and crack
16 density, as presented in Fig. 16. In case of a scan speed of 2100 mm/s and a doubled layer
17 thickness, the crack density is close to the one obtained in section 3.2 with a beam spot of 132
18 μm . Independent of the scan velocity, the Archimedean density is quite low. With a decreased
19 scan velocity, the Archimedean density increases, but simultaneously the amount of cracks. The
20 reason could be found in deeper melt pools, which are required to produce more base or bulk
21 material, in case of a doubled layer thickness. At the same time, more re-melting cracks are
22 generated due to an increased melt pool depth, as investigated in section 3.1. In case of an
23 additionally increased hatch distance of 50%, the Archimedean density drops even more, as
24 shown in Fig. 17 with varying scan speeds. Further investigations are needed, to find an
25 optimum with increased layer thickness and hatch distance.



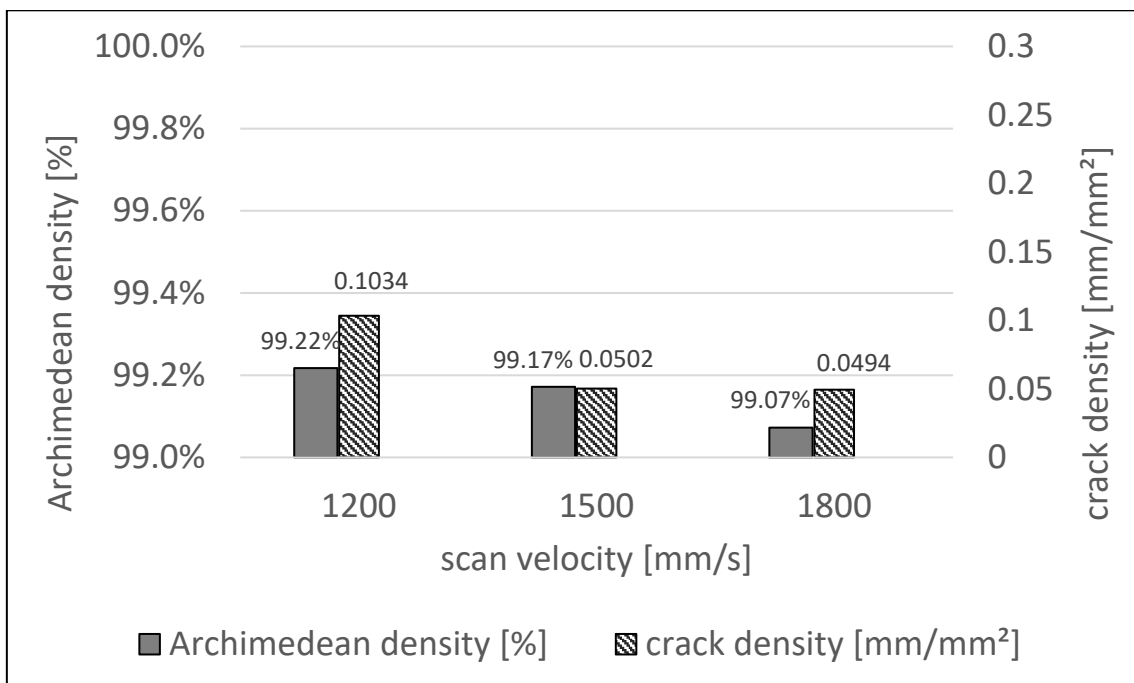
1

2

3

4

Fig. 16: defect analysis results with varying laser scan velocities, in case of 600 W laser power, a beam diameter of 156 μm and a doubled layer thickness of 60 μm



5

6

7

Fig. 17: defect analysis results with varying laser scan velocities, in case of 600 W laser power, a beam diameter of 156 μm , a doubled layer thickness of 60 μm and an increased hatch distance by 50%

1 4. Conclusion

2 Using the same maximum laser intensity of 62876 W/mm^2 and line energy of 0.25 J/mm ,
3 as received from dense and crack-free SLM- processed C247LC samples with 200 W power,
4 similar results are obtained regarding Archimedean density and crack density with an increased
5 beam diameter in case of 600 W power and a scan velocity of 2400 mm/s. The productivity can
6 be increased relatively by 300%. A melt pool depth range from $66 \mu\text{m}$ to $81 \mu\text{m}$ is discovered,
7 where not only solidification cracks can be avoided, but also re-melting cracks, which result
8 from higher laser power inputs. Based on dimensional analysis, a model is described and
9 presented, which combines the samples density with the crack density through the melt pool
10 depth. The model includes six main and two additional process and laser parameters. Results
11 from the model and the experimental measured values are in good agreement. Furthermore, the
12 influence of a doubled layer thickness and additionally increased hatch distance by 50% with
13 different laser scan speeds on the Archimedean density and crack density is investigated. In
14 case of a doubled layer thickness, not only the Archimedean density increases with a decreased
15 scan velocity, but also the crack density. Since deeper melt pools are required to produce more
16 base or bulk material for that case, also more re-melting cracks are generated, at the same time.
17 Combining a doubled layer thickness with an increased hatch distance by 50%, the
18 Archimedean density drops even more. Further investigations are needed, to find an optimum
19 regarding highly increased layer thickness, Archimedean density and crack density.

20

21 Acknowledgements

22 The authors would like to thank the Swiss Innovation Agency Innosuisse for financial
23 support in the frame of project 25357.2 PFNM-NM, Kai Gutknecht and Alex Frauchiger, for
24 their support at the laboratory machine.

25

26 Declarations

27 **Funding:** Open Access funding provided by ETH Zurich. This study was funded by the
28 Swiss Innovation Agency Innosuisse in the frame of project 25357.2 PFNM-
29 NM.

30

31 **Competing Interests:** The authors declare no competing interests.

32

33

34

1 **Author Contributions**

- 2 **Marcel Gerstgrasser:** Conceptualization, Methodology, Investigation, Writing -
 3 Original Draft, Visualization, Software, Validation, Formal
 4 analysis
- 5 **Michael Cloots:** Conceptualization
- 6 **Raphael Jakob:** Data Curation, Writing - Review & Editing, Formal analysis
- 7 **Josef Stirnimann:** Project administration
- 8 **Konrad Wegener:** Supervision, Writing - Review & Editing

9
10

11 **References**

- 12 [1] Montero-Sistiaga, M.L., Godino-Martinez, M., Boschmans, K., Kruth, J.-P., Van Humbeeck, J.,
 13 Vanmeensel, K. (2018). Microstructure evolution of 316L produced by HP-SLM (high power selective
 14 laser melting). *Additive Manufacturing* 23, pp. 402-410.
- 15 [2] Sun, Z., Tan, X., Tor, S.B., Yeong, W.Y. (2016). Selective laser melting of stainless steel 316L with low
 16 porosity and high build rates. *Materials & Design* 104, pp. 197-204.
- 17 [3] Metelkova, J., Kinds, Y., Kempen, K., de Formanoir, C., Witvrouw, A., Van Hooreweder, B. (2018).
 18 On the influence of laser defocusing in Selective Laser Melting of 316L. *Additive Manufacturing* 23, pp.
 19 161-169.
- 20 [4] Bang, G.B., Kim, W.R., Kim, H.K., Park, H.-K., Kim, G.H., Hyun, S.-K., Kwon, O., Kim, H.G. (2021). Effect
 21 of process parameters for selective laser melting with SUS316L on mechanical and microstructural
 22 properties with variation in chemical composition. *Materials & Design* 197, pp. 109221.
- 23 [5] Makoana, N.W., Yadroitsava, I., Möller, H., Yadroitsev, I. (2018). Characterization of 17-4PH single
 24 tracks produced at different parametric conditions towards increased productivity of LPBF systems—
 25 the effect of laser power and spot size upscaling. *Metals* 8, pp. 475.
- 26 [6] Zuo, P., Chen, S., Wei, M., Zhou, L., Liang, J., Liu, C., Wang, M. (2019). Microstructure evolution of
 27 24CrNiMoY alloy steel parts by high power selective laser melting. *Journal of Manufacturing Processes*
 28 44, pp. 28-37.
- 29 [7] Jing, G., Huang, W., Yang, H., Wang, Z. (2020). Microstructural evolution and mechanical properties
 30 of 300M steel produced by low and high power selective laser melting. *Journal of Materials Science &*
 31 *Technology* 48, pp. 44-56.
- 32 [8] Gunenthiram, V., Peyre, P., Schneider, M., Dal, M., Coste, F., Fabbro, R. (2017). Analysis of laser–
 33 melt pool–powder bed interaction during the selective laser melting of a stainless steel. *Journal of*
 34 *Laser Applications* 29, pp. 022303.
- 35 [9] Jing, G., Wang, Z. (2021). Defects, densification mechanism and mechanical properties of 300M
 36 steel deposited by high power selective laser melting. *Additive Manufacturing* 38, pp. 101831.

- 1 [10] Buchbinder, D., Schleifenbaum, H., Heidrich, S., Meiners, W., Bültmann, J. (2011). High power
2 selective laser melting (HP SLM) of aluminum parts. *Physics Procedia* 12, pp. 271-278.
- 3 [11] Wischeropp, T.M., Tarhini, H., Emmelmann, C. (2020). Influence of laser beam profile on the
4 selective laser melting process of AlSi10Mg. *Journal of Laser Applications* 32, pp. 022059.
- 5 [12] Rashid, R.R., Ali, H., Palanisamy, S., Masood, S. (2017). Effect of process parameters on the surface
6 characteristics of AlSi12 samples made via Selective Laser Melting. *Materials Today: Proceedings* 4, pp.
7 8724-8730.
- 8 [13] Shi, W., Liu, Y., Shi, X., Hou, Y., Wang, P., Song, G. (2018). Beam diameter dependence of
9 performance in thick-layer and high-power selective laser melting of Ti-6Al-4V. *Materials* 11, pp. 1237.
- 10 [14] Soylemez, E. (2020). High deposition rate approach of selective laser melting through defocused
11 single bead experiments and thermal finite element analysis for Ti-6Al-4V. *Additive Manufacturing* 31,
12 pp. 100984.
- 13 [15] Mathe, N.R., Tshabalala, L.C., Hoosain, S., Motibane, L., du Plessis, A. (2021). The effect of porosity
14 on the mechanical properties of Ti-6Al-4V components manufactured by high-power selective laser
15 melting. *The International Journal of Advanced Manufacturing Technology*, pp. 1-9.
- 16 [16] Montero-Sistiaga, M.L., Pourbabak, S., Van Humbeeck, J., Schryvers, D., Vanmeensel, K. (2019).
17 Microstructure and mechanical properties of Hastelloy X produced by HP-SLM (high power selective
18 laser melting). *Materials & Design* 165, pp. 107598.
- 19 [17] Yang, H., Meng, L., Luo, S., Wang, Z. (2020). Microstructural evolution and mechanical
20 performances of selective laser melting Inconel 718 from low to high laser power. *Journal of Alloys and
21 Compounds* 828, pp. 154473.
- 22 [18] Wang, Y., Shi, J. (2020). Developing very strong texture in a nickel-based superalloy by selective
23 laser melting with an ultra-high power and flat-top laser beam. *Materials Characterization* 165, pp.
24 110372.
- 25 [19] Sow, M., De Terris, T., Castelnau, O., Hamouche, Z., Coste, F., Fabbro, R., Peyre, P. (2020). Influence
26 of beam diameter on Laser Powder Bed Fusion (L-PBF) process. *Additive Manufacturing* 36, pp.
27 101532.
- 28 [20] Yin, J., Yang, L., Yang, X., Zhu, H., Wang, D., Ke, L., Wang, Z., Wang, G., Zeng, X. (2019). High-power
29 laser-matter interaction during laser powder bed fusion. *Additive Manufacturing* 29, pp. 100778.
- 30 [21] Carter, L.N., Attallah, M.M., Reed, R.C. (2012). Laser powder bed fabrication of nickel-base
31 superalloys: influence of parameters; characterisation, quantification and mitigation of cracking.
32 *Superalloys 2012*, pp. 577-586.
- 33 [22] Gerstgrasser, M., Cloots, M., Stirnimann, J., Wegener, K. (2021). Focus shift analysis, to
34 manufacture dense and crack-free SLM-processed CM247LC samples. *Journal of Materials Processing
35 Technology* 289, pp. 12.
- 36 [23] Gerstgrasser, M., Cloots, M., Stirnimann, J., Wegener, K. (2021). Residual stress reduction of LPBF-
37 processed CM247LC samples via multi laser beam strategies. *The International Journal of Advanced
38 Manufacturing Technology*, pp.
- 39 [24] Wirth, F., Frauchiger, A., Gutknecht, K., Cloots, M. (2021). Influence of the Inert Gas Flow on the
40 Laser Powder Bed Fusion (LPBF) Process. Springer International Publishing, Cham, pp. 192-204.

- 1 [25] Gutknecht, K., Haferkamp, L., Cloots, M., Wegener, K. (2020). Determining process stability of
2 Laser Powder Bed Fusion using pyrometry. *Procedia CIRP* 95, pp. 127-132.
- 3 [26] Poprawe, R., Boucke, K., Hoffman, D. (2018). *Tailored Light 1: High Power Lasers for Production*.
4 Springer.
- 5 [27] Koechner, W. (2006). *Solid-State Laser Engineering*.
- 6 [28] Mosallanejad, M., Niroumand, B., Aversa, A., Manfredi, D., Saboori, A. (2021). Laser Powder Bed
7 Fusion in-situ alloying of Ti-5% Cu alloy: Process-structure relationships. *Journal of Alloys and*
8 *Compounds* 857, pp. 157558.
- 9 [29] Rosenthal, D. (1941). Mathematical theory of heat distribution during welding and cutting.
10 *Welding journal* 20, pp. 220-234.
- 11 [30] Promoppatum, P., Yao, S.-C., Pistorius, P.C., Rollett, A.D. (2017). A Comprehensive Comparison of
12 the Analytical and Numerical Prediction of the Thermal History and Solidification Microstructure of
13 Inconel 718 Products Made by Laser Powder-Bed Fusion. *Engineering* 3, pp. 685-694.
- 14 [31] Tang, M., Pistorius, P.C., Beuth, J.L. (2017). Prediction of lack-of-fusion porosity for powder bed
15 fusion. *Additive Manufacturing* 14, pp. 39-48.
- 16 [32] Khan, K., Mohr, G., Hilgenberg, K., De, A. (2020). Probing a novel heat source model and adaptive
17 remeshing technique to simulate laser powder bed fusion with experimental validation.
18 *Computational Materials Science* 181, pp. 109752.
- 19 [33] Estrada-Díaz, J.A., Elías-Zúñiga, A., Martínez-Romero, O., Rodríguez-Salinas, J., Olvera-Trejo, D.
20 (2021). A Mathematical Dimensional Model for Predicting Bulk Density of Inconel 718 Parts Produced
21 by Selective Laser Melting. *Materials* 14, pp. 512.
- 22 [34] Estrada-Díaz, J.A., Elías-Zúñiga, A., Martínez-Romero, O., Olvera-Trejo, D. (2021). Enhanced
23 Mathematical Model for Producing Highly Dense Metallic Components through Selective Laser
24 Melting. *Materials* 14, pp. 1571.
- 25 [35] Zohuri, B. (2015). *Dimensional analysis and self-similarity methods for engineers and scientists*.
26 Springer.
- 27 [36] Jazar, R.N. (2020). *Approximation methods in science and engineering*. Springer Nature.
- 28 [37] Dym, C. (2004). *Principles of mathematical modeling*. Elsevier.
- 29 [38] Mahamood, R.M., Akinlabi, E.T., Shukla, M., Pityana, S. (2013). Characterizing the effect of laser
30 power density on microstructure, microhardness, and surface finish of laser deposited titanium alloy.
31 *Journal of Manufacturing Science and Engineering* 135, pp.
- 32 [39] Gerstgrasser, M., Smolenicki, D., Akbari, M., Klippel, H., Roelofs, H., Cadoni, E., Wegener, K. (2021).
33 Analysis of two parameter identification methods for original and modified Johnson-Cook fracture
34 strains, including numerical comparison and validation of a new blue-brittle dependent fracture model
35 for free-cutting steel 50SiB8. *Theoretical and Applied Fracture Mechanics* 112, pp. 102905.
- 36
- 37